Chapter 5
Two-Dimensional (2D) Damage Percolation Modeling

As discussed in the preceding chapters, the second phase particle field in a dispersion strengthened ductile material can be described as a random distribution displaying a certain level of particle clustering (Pilkey et al. 1995). Ordinary unit cell models such as Gurson's (1977) analytical model or other numerical unit cell models (e.g. Needleman 1972; Worswick 1988) with a uniformly distributed particle/void field are unable to capture microstructures that are random and/or clustered. In order to overcome this disadvantage of unit cell models when applied to real micro-defects, Benson (1995) used a two-dimensional unit cell calculation to investigate the effect of void cluster size on ductile fracture. In his study, a unit cell with randomly distributed void clusters was modelled. Thomson et al. (1999) proposed a numerical unit cell model that contains a single particle cluster. Unfortunately, this model still possesses a periodic particle field. Real microstructures always display a random particle distribution with some superimposed degree of particle clustering. Therefore, it is doubtful that unit cell calculations are able to capture the onset of ductile fracture in real materials.

A new approach to predicting ductile damage evolution, known as the damage percolation model, has been proposed by Pilkey et al. (1998) and Worswick et al. (2001) to address this issue. In this approach, measured second phase particle fields are used as the starting point to capture the real variation in inter-particle spacing. The particle field is subjected to some uniform, remote strain field and damage nucleation and growth models are applied discretely to each particle in the field. Void coalescence is predicted as the merging of nearest-neighbouring voids and generally initiates within void clusters. Large-scale cracking is predicted once two or more clusters of voids coalesce, causing a chain reaction of profuse coalescence and gross material failure.

The damage percolation approach is the focus of this book and this chapter presents the theoretical framework for this methodology. One important issue in the damage percolation approach is the determination of the minimum particle field size or representative volume element (RVE) required to capture the bulk material response. This issue is addressed in this chapter, within the framework of a uniform

strain assumption. The introduction of strain gradients within the damage percolation approach is addressed in the following chapter in which the damage percolation model is coupled with a FE model.

5.1 The Damage Percolation Model

The starting point for the damage percolation model is the second phase particle field. This is usually obtained using image analysis of digital micrographs acquired directly from an optical microscope. Tessellation methods are applied to characterize second phase particle fields and the degree of clustering present in the microstructure. Matrix erosion tessellation techniques are employed to extract the degree of clustering present in the as-received alloys which contain a dispersion of Fe- and Mn-based inter-metallic particles (Pilkey 1997). The tessellated particle fields are read into the damage percolation model to simulate the development of damage under sheet forming conditions. Of particular interest are the conditions at which particle-nucleated void damage links up and the extent of linkage required to produce unstable crack growth and final fracture.

Annealed, O-temper AA5182 aluminum alloy sheets is considered in this chapter. This alloy is a candidate for use in automotive inner body panels as lightweight replacement for conventional steel. A plan view section of the as-received microstructure was prepared for metallographic examination and image analysis. The AA5182 microstructure has a dual population of Fe and Mn intermetallic particles. For simplicity, no attempt was made to distinguish between these different particle types during the acquisition and processing of the particle fields.

5.1.1 Particle Field Tessellations

A large-scale high-resolution digital image of a second-phase particle field was acquired from the planar metallographic view. This massive particle field image is roughly $5,500 \times 4,250$ pixels in size and has a resolution of 0.372 μm/pixel, corresponding to a physical size of about 2.0×1.6 mm. The constituent particles have been separated from the matrix background using standard thresholding techniques.

Relevant particle and clustering characteristics have been extracted from the large-scale high-resolution particle fields through the application of a matrix erosion tessellation algorithm. Large-scale image of the matrix erosion tessellation produced for the AA5182 microstructure is shown in Fig. 5.1.

Particle field feature data generated by the tessellation software is read directly by the damage percolation software. This model considers the nucleation and growth of voids at individual particles within the microstructure. Coalescence of individual voids to form cracks and the subsequent growth of cracks and
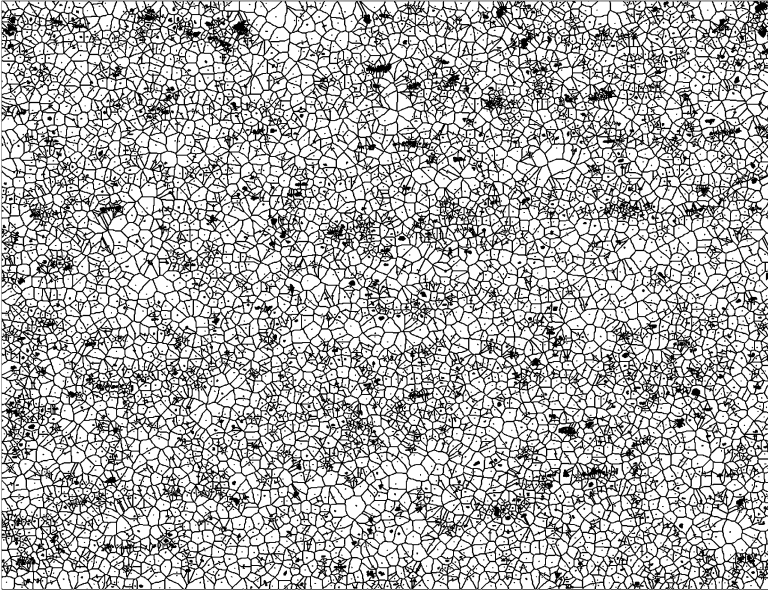
Fig. 5.1 A 5,500 × 4,250 pixel large-scale tessellated second phase particle field of Al-Mg alloy AA5182 used in the RVE study (RD, horizontal; TD, vertical) (Chen 2004)

coalescence of cracks with other cracks or isolated voids is also modelled (Worswick et al. 1998). Particle feature data utilized by the model includes:

- particle centroid coordinates
- particle principal axes (and orientation)
- nearest neighbour list
- cluster list (particles comprising each cluster)

5.1.1.1   Inter-Particle Dilational Spacing (IPDS)

The tessellation software calculates the so-called inter-particle dilational spacing (IPDS) for each tessellated particle field. In these particle clustering studies, a combination of matrix erosion tessellation and dilational counting techniques, previously employed by Shehata and Boyd (1988), were applied to the acquired particle fields (Pilkey et al. 1998). During each particle dilation step, the software records when each particle feature merges or touches another dilating particle feature. First contact or agglomeration between a particle and one of its neighbours defines then a nearest neighbour. Knowing the pixel size, the software can then determine the nearest neighbour spacing based upon the number of dilations performed. Dilational counting measures are then tabulated during the construction of a matrix erosion spatial tessellation and represented by a histogram of inter-
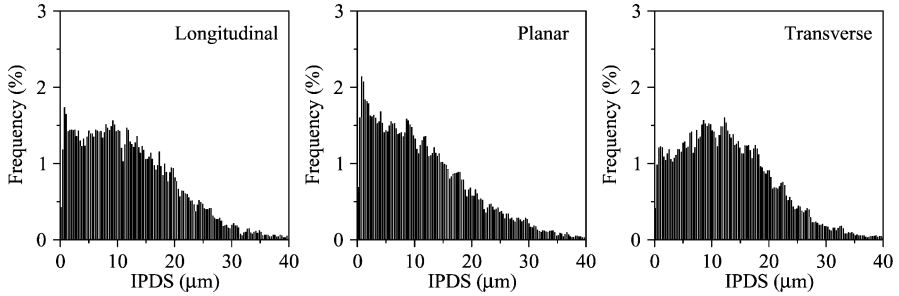
Fig. 5.2 Interparticle dilitational spacing (IPDS) of AA5182 sheets in different view planes

particle dilational spacing (IPDS) frequencies. Given that a matrix erosion tessellation algorithm involves repeated particle dilational passes, equivalent to matrix erosion passes, the number of distinct features that disappear from the particle field during each dilation pass is recorded as a frequency. The disappearance of a feature occurs when it agglomerates with another feature (i.e. dilating neighbours come in contact). At the start of the spatial tessellation process, each particle represents a feature. By recognizing that each particle dilation pass is of characteristic length in a digital image, the agglomeration frequencies can be plotted against dilational distance to produce an IPDS frequency spectrum. It follows that local peaks in the frequency of dilational merging events are indicative of characteristic spacings within the tessellated particle field. The dilating features which agglomerate at the smallest of these characteristic spacings are referred to as first order clusters, while successive IPDS peaks signify so-called second, third and higher orders of particle clusters. Figure 5.2 shows the IPDS histograms for the 1.0 mm AA5182 sheet in three view planes.

For mathematical convenience, individual particles are represented as ellipses with principal axes aligned with the sheet rolling and transverse directions. Thus any tilting of particles relative to these axes was neglected. In general, an ellipse representation of particles is considered acceptable and greatly simplifies particle interaction and void growth calculations.

5.1.1.2 Particle Aspect Ratio

Particle aspect ratio values were obtained by modelling each particle as an ellipse with equivalent second moments of area. Particles with a major axis aligned more closely to the longitudinal direction are assigned aspect ratios greater than unity. Particles with aspect ratios in excess of 2 or less than ½ are referred to here as high aspect ratio particles. Figure 5.3 shows the histograms of particle aspect ratio for the 1.0 mm AA5182 sheet in three view planes.
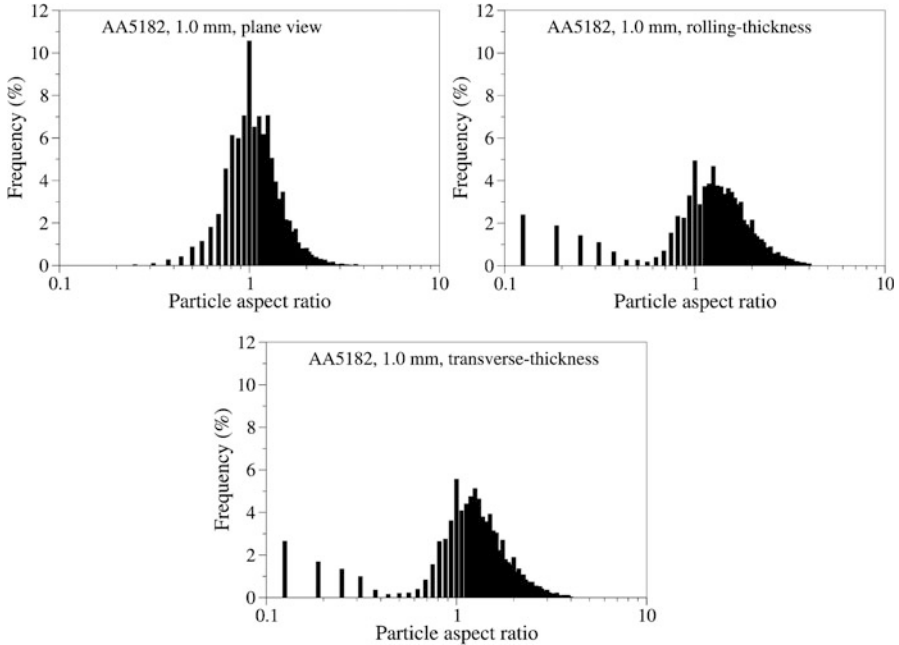
Fig. 5.3 Normalized histograms of particle aspect ratio: AA5182. Aspect ratios greater than unity indicates particles oriented longitudinally

5.1.1.3 Paricle Size

The particle size distribution is an important microstructural parameter impacting ductile fracture. Figure 5.4 shows the measured particle size distributions for a 1.0 mm AA5182 sheet. In the figure, particle size is plotted in terms of particle area in the section plane.

5.1.2 Damage Evolution Predictions

Damage evolution was treated as consisting of three distinct stages: void nucleation, growth, and coalescence. The first and last stages, nucleation and coalescence are typically the least quantified in terms of actual measurements or model predictions.

5.1.2.1 Void Nucleation

Void nucleation was treated as strain controlled and as being sensitive to particle size (Brown and Embury 1973; Teirlinck et al. 1985; Le Roy et al. 1981; Fisher and
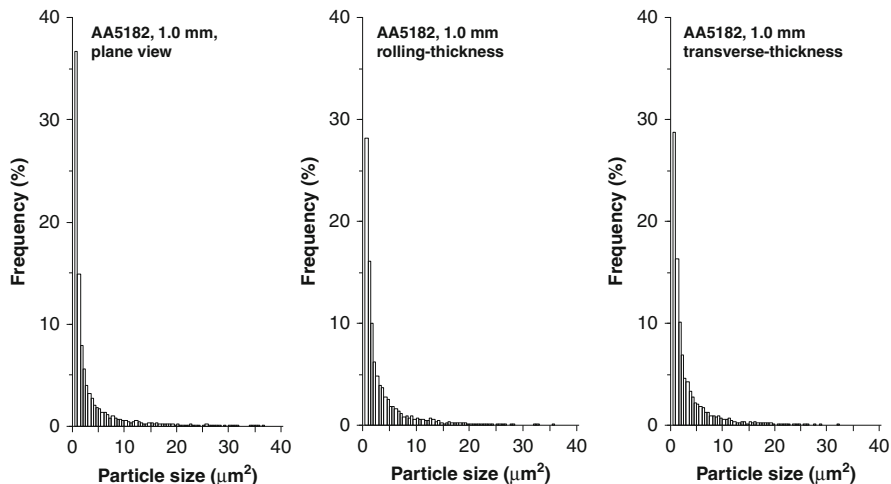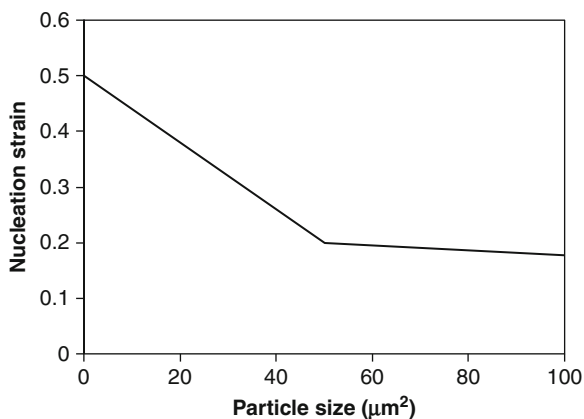
Fig. 5.4 Normalized histograms of particle size: AA5182

Fig. 5.5 Particle size-controlled void nucleation criterion adopted for both alloys studied (Reprinted with permission from Worswick et al. 2001)


Gurland 1981a, b). In general, nucleation is assumed to occur preferentially at larger particles and the fraction of nucleated smaller particles increases with strain. This treatment is consistent with the model suggested by Embury (1985), in which void nucleation "sweeps" through a particle population initiating preferentially at larger particles. Figure 5.5 plots the void nucleation strain as a function of particle size (area) proposed by Worswick et al. (1998, 2001) and adopted in the RVE size study for both alloys.

5.1.2.2   Void Growth

Void growth was modelled using results from unit cell calculations by Thomson et al. (1999). In that work, the critical geometric parameters governing void growth

Fig. 5.6 Schematic of idealized void interaction geometry: (**a**) aligned or longitudinal case (**b**) transverse case
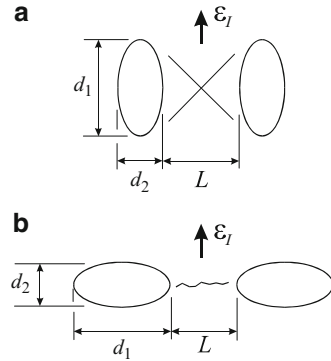
rate have been identified as void aspect ratio and degree of clustering. There was also a strong interaction between these geometric parameters and the strain state. Under plane strain conditions, for example, void growth was greatest when the first principal strain direction was perpendicular to the major axis of a void stringer or an elongated single void.

The current void growth treatment in the percolation damage model considers void aspect ratio and strain state, and utilizes void growth rates determined from isolated void, unit cell simulations. Clustering effects on rate of void growth are not considered at present. This simplification is somewhat justified since the behaviour of a void stringer was shown to be similar to an isolated void of similar size as the stringer. Once the flow stress in the inter-void ligament becomes saturated, the stringer "grows" much as an elongated void (Worswick et al. 1998). In the percolation damage model, the voids in a stringer-like cluster coalesce rapidly, after which they would be treated as a single larger ellipsoidal void.

Once nucleated, individual voids were assumed to grow at the prescribed rates predicted from the unit cell calculations of Thomson et al. (1999). It was assumed that after nucleation, the entire particle could be treated as void. Void growth under conditions of partial void-matrix separation should be considered in future work. Prior to nucleation, particles are assumed to deform at the bulk deformation rate of the matrix.

5.1.2.3   Void Coalescence

Void coalescence was predicted using a modified version of Brown and Embury's (1973) ligament-to-void-size-ratio criterion. Criteria based on plastic zone size, such as used by Dubensky and Koss (1987), were not employed, primarily because the strains in the matrix were very large and coalescence in the materials modelled occurs well after impingement of plastic zones surrounding neighbouring voids.

The inter-void geometry considered by Brown and Embury (1973) is depicted in Fig. 5.6a. Void coalescence is said to occur through shear band development

Fig. 5.7 Schematic of
interaction geometry adopted
in current work
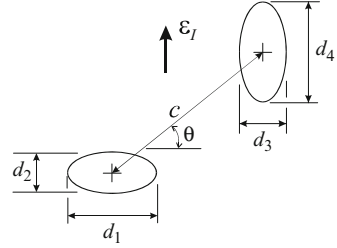
between two neighbouring elongated voids when the ratio of remaining ligament, L, to void length, d_2, drops below a critical value, γ:

$$\frac{L}{d_2} < \gamma \qquad (5.1)$$

Typically, the value of γ is taken as unity or can be related to the stress state as in Weck (2006).

Brown and Embury's (1973) model was originally developed for the case of loading along the axis of elongated particles or voids as in Fig. 5.6a. This geometry applies naturally to so-called longitudinal load cases, however, the geometry for transverse loading is quite different, as shown in Fig. 5.6b. Applying Eq. (5.1) to this geometry would require that voids be positioned extremely close together before coalescence will occur since the "interaction length", L, is based on the void dimension measured along the principal straining direction. This length seems excessively small since voids elongated transverse to the ε_I-direction will experience a severe strain and stress concentration at their "poles". This effect was demonstrated by Thomson et al. (1999) using unit cell models in which inter-ligament plastic collapse appears to be the coalescence mechanism under transverse loading conditions. Based on these observations, a larger interaction distance may be more appropriate than that given by Eq. (5.1).

As a simple first step, it was decided to use

$$\frac{L}{\max(d_1, d_2)} < \gamma \qquad (5.2)$$

in which the term in the denominator is the maximum of the two in-plane axes of the void. This approach extends the interaction distance for transverse loading while maintaining the Brown and Embury (1973) criterion for longitudinal loading. In all cases, γ was taken as unity, although γ may also be a function of stress or strain state as noted by Sun (1991) for triaxial stress states.

Other geometrical differences arise in comparing actual particle fields with the idealised geometries. These include differing sizes of the interacting particles as well as ligament orientations that are non-orthogonal to the ε_I-direction as depicted in Fig. 5.7.

Fig. 5.8 A crack formed by
coalescence of two
neighbouring voids
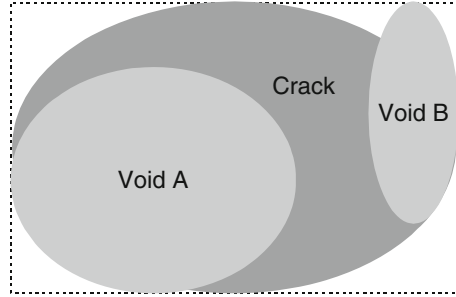
The approach used in this work was to define an average particle size, D, as

$$D = \frac{\max(d_1, d_2) + \max(d_3, d_4)}{2} \tag{5.3}$$

and a ligament size as

$$L = c - D \tag{5.4}$$

where c is the void centre-to-centre distance and d_1, d_2, d_3 and d_4, are the void dimensions given in Fig. 5.7. Coalescence is said to occur, then, when

$$\frac{L}{D} < \gamma \tag{5.5}$$

A final restriction is placed on ligament orientation to determine whether coalescence can occur,

$$\theta < \theta_{\max} \tag{5.6}$$

where $\theta_{\max}$ is taken as 45°. In cases where θ exceeds $\theta_{\max}$, one would expect the ligament to be shielded from deformation by the voids. This requirement was enforced for the uniaxial calculations, but not for the stretch condition in which the in-plane loading is symmetric.

The search algorithm used to predict void coalescence utilizes the nearest neighbour list generated by the tessellation software. With each strain increment, Eqs. (5.3, 5.4, 5.5 and 5.6) are applied to all neighbouring pairs of nucleated voids.

5.1.2.4 Post-coalescence Treatment

Once two voids coalesce, they are treated as a single larger void or "crack", as shown in Fig. 5.8. Note that the term crack is used here for convenience and does not imply a sharp-tipped crack in a fracture mechanics sense. Propagation of damage can then proceed at three levels: (i) further coalescence of isolated voids; (ii) coalescence of isolated voids with existing cracks; and (iii) coalescence of two

or more existing cracks. All of these processes can be expected to occur concurrently during continuing deformation.

Two approaches are possible to handle coalescence of voids with cracks or cracks with cracks. One approach would be to treat cracks as collections of isolated voids and to apply Eqs. (5.3, 5.4, 5.5 and 5.6) to every void-void pairing defined by the list(s) of voids in the crack(s) and their respective neighbour lists. The major drawback of this approach is that it neglects the amplification of effective void size and interaction distance occurring when one or more voids coalesce to form a larger void.

To account for this amplification effect, a different approach was used in which groups of coalesced voids were treated as a single larger elliptical void. The size of this elliptical void is such that its "bounding rectangle" encloses all voids comprising the crack (Fig. 5.8). Once established, this elliptical crack can then grow and coalesce with other voids or cracks. The significant increase in size of this crack serves to introduce the amplification of the interaction distance one would expect to occur with the onset of void coalescence.

5.2 Damage Predictions

In this section, the percolation model is demonstrated by simulating the damage evolution in AA5182 aluminum alloy sheet. Two loading conditions are considered, biaxial stretching and uniaxial stress. The uniaxial loading case is applied in two directions relative to the particle field, longitudinal and transverse. In rolling aluminum alloy sheet, second phase particles tend to elongate and align in stringers oriented along the rolling direction. Thus the longitudinal case in Fig. 5.6a corresponds to loading along the sheet rolling direction whereas the transverse case (Fig. 5.6b) represents in-plane loading perpendicular to the rolling direction. In the current study, loading was restricted to either equi-biaxial stretching ($\varepsilon_2/\varepsilon_1 = 1$) or uniaxial stress ($\sigma_2 = \sigma_3 = 0$) along the longitudinal or transverse directions. A strain step of 0.25 % is adopted in the damage percolation simulations for all three loading cases. The biaxial case corresponds to the highest triaxiality prior to necking of the sheet for which damage rates are higher. The uniaxial case is of interest since it corresponds to the stress state acting along the circumference of the stretch flange cutout (see Chap. 2). Damage variation is plotted in terms of void areal fraction, nucleated void areal fraction, areal fraction of voids in cracks and crack areal fraction to characterize the damage evolution in different stages. Also captured is the sequence of particle field evolution under various loading cases.

5.2.1 Damage Evolution

Figure 5.9 shows a typical sequence of predicted damage at various strain levels prior to fracture under biaxial stretch loading of AA5182 sheet, using a smaller
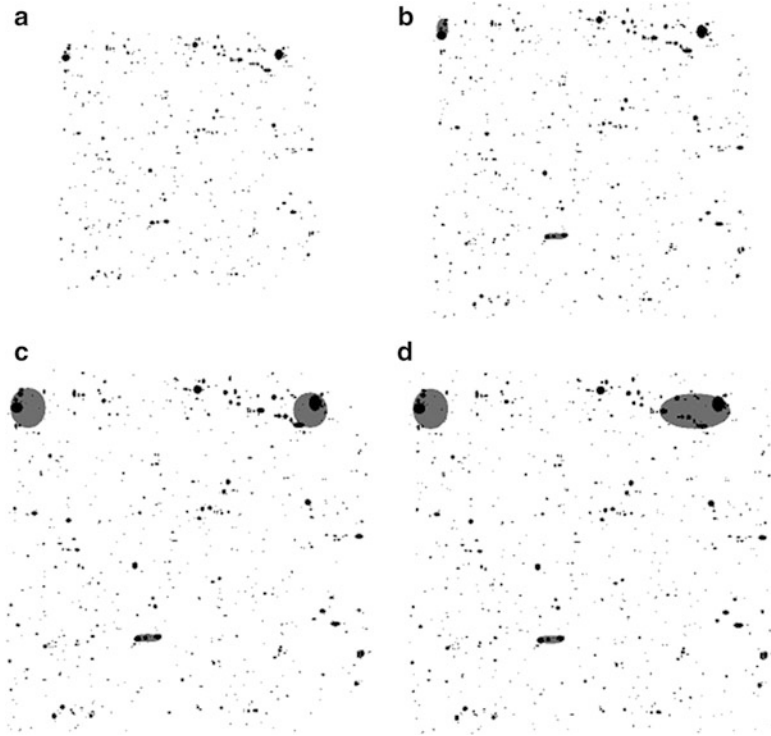
Fig. 5.9 Predicted damage for AA5182 under equi-biaxial strain conditions, 2,000 × 2,000 pixels (2,000a): (**a**) initial particle field; (**b**) 20 % strain; (**c**) 33.75 % strain; and (**d**) 34 % strain

2,000 × 2,000 pixel particle field extracted from the larger field in Fig. 5.1. The particles are shaded black and the approximate sizes of cracks are represented as grey ellipses sized to fit within the bounding box encompassing all voids within a crack. This ellipse corresponds to the "crack size" used to determine void-crack and crack-crack coalescence.

Using the adopted interaction criteria/assumptions, damage propagation becomes very dependent upon the nucleation process. Damage commences with the larger particles at a strain of roughly 19 % with local regions of void coalescence forming almost immediately at strain levels of 20 % (Fig. 5.9b). Damage progresses with nucleation of new voids which then allows formation of new cracks and growth of existing cracks, largely confined to the original particle clusters. At a much larger strain of 33.75 % (Fig. 5.9c), further void coalescence has occurred and several larger cracks are observed; however, the damage is still confined to within at most three neighbouring particle clusters. Larger cracks can only form once neighbouring cracks become large enough to bridge inter-crack ligaments (Fig. 5.9d). This process is very sensitive to void nucleation as well as void and crack interaction since the extension of cracks requires the introduction of new voids to sustain growth. At a strain of 34 % (Fig. 5.9d), the crack size becomes
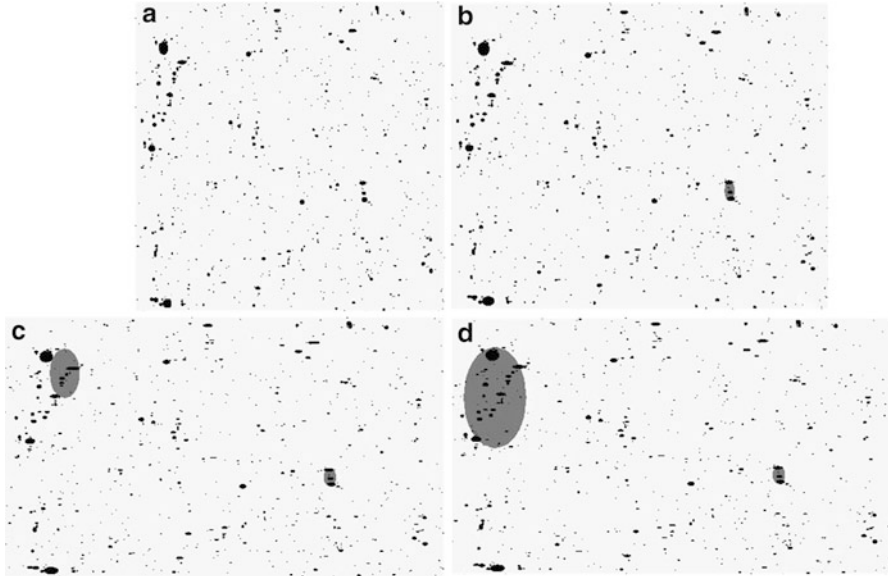
Fig. 5.10 Predicted damage for AA5182 under transverse uniaxial stress conditions, 2,000 × 2,000 pixels (2,000a): (**a**) initial particle field; (**b**) 20 % strain; (**c**) 35 % strain; and (**d**) 36 % strain

critical and the linkage of four or more clusters of voids triggers a chain reaction in which crack coalescence propagates across the field without further straining (not shown).

Figure 5.10 shows the sequence of predicted damage at various strain levels prior to fracture for the same initial particle field under transverse uniaxial stress. Once again voids nucleate and coalesce within the same clusters having larger particles. However, it is observed that in Fig. 5.10, nucleation and coalescence of particles within a particle cluster on the bottom left of the field didn't happen until fracture. This behaviour is different from what was observed for the biaxial stretching case, which can be attributed to the constraint on the coalescence path given by Eq. (5.6) for uniaxial loading. This effectively reduces the number of nearest neighbours that can coalesce compared to the equi-biaxial case.

5.2.2   Predicted Damage Rates

The predicted damage-strain history for AA5182 under equi-biaxial stretch conditions using a 4,000 × 4,000 pixel particle field is plotted in Fig. 5.11. Predicted damage histories under uniaxial stress loading for AA5182 are shown in Fig. 5.12. Results are shown for both longitudinal and transverse loading in

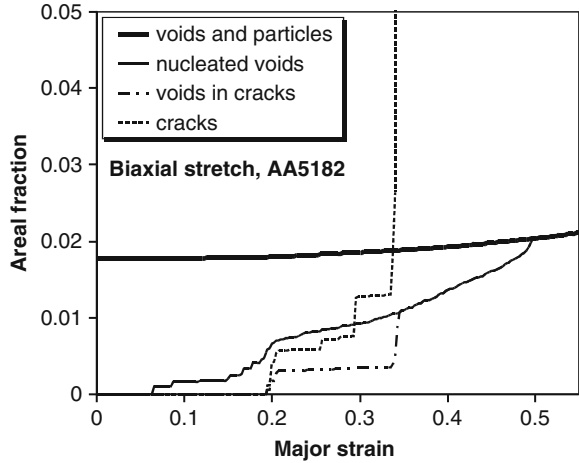**Fig. 5.11** Damage development under biaxial stretching, AA5182

Fig. 5.12 Damage development for AA5182 under (**a**) longitudinal uniaxial stress conditions and (**b**) transverse uniaxial stress conditions
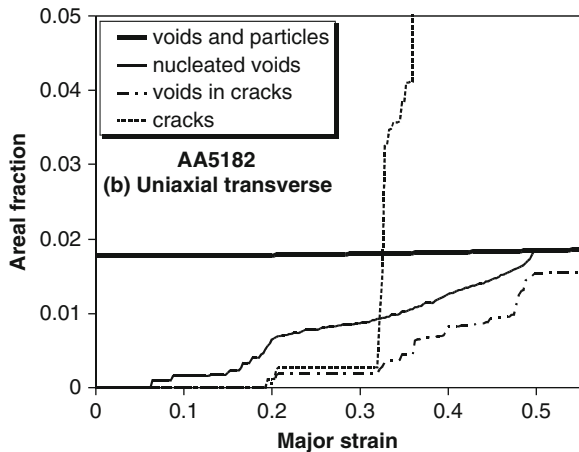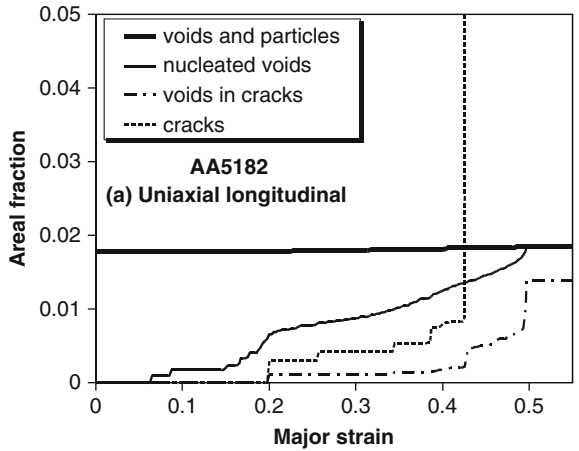
Fig. 5.12a, b, respectively. Damage development proceeds more rapidly for the transverse case. Furthermore, a much lower strain of 36.25 % is predicted for profuse void coalescence under transverse loading compared to 42.75 % for the longitudinal direction. This behaviour is attributed to the nature of the particle stringers which are aligned with the rolling direction (Fig. 5.1), providing an easier coalescence path under transverse loading conditions.

The rate of void growth is higher for the stretch cases compared to the uniaxial cases. This observation stems from the steeper slope of the solid curve in Fig. 5.11 (stretch case) compared to the uniaxial growth rates seen in Fig. 5.12. This orientation effect is attributed to the high propensity for large, oriented stringer-like clusters in AA5182 (Fig. 5.1).

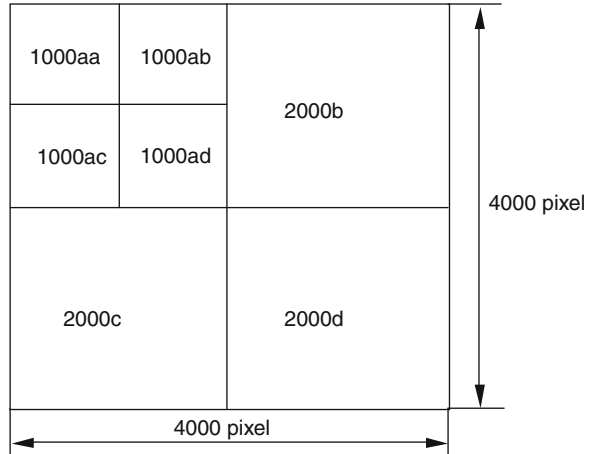## 5.3 Selection of Representative Volume Element (RVE)

Determination of the representative volume element (RVE) of a microstructure is essential in the micro-mechanics study of ductile fracture. As well-verified by numerous researchers (Tvergaard 1990; Meyers and Aimone 1983; Tvergaard and Needleman 1986, 1997; Needleman and Tvergaard 1991), ductile fracture is a very localized phenomenon. Therefore, it was decided to investigate the effect of RVE size, that is, the size of the region of sampled material, on the predicted onset of ductile fracture. Of particular interest was the effect of a reduction in RVE size on the predicted failure strain. Here, the RVE can be thought of as the minimum size of particle field required to obtain a repeatable prediction of damage development. In this manner, the predictions are no longer dependent upon the choice of the particle field. In addition, determination of the minimum required field size also makes the predictions more efficient, as well as the image acquisition operation which can be tedious.

The approach taken here is to study the influence of particle field size on the onset of profuse coalescence. Predictions are performed first using a large image containing many particles; these are the simulations presented in the preceding section of this chapter. Next the images are progressively subdivided into smaller images and the damage percolation simulations are repeated for each sub-image or particle field. This process of image-subdivision is repeated until the profuse void coalescence strain begins to vary significantly for the smallest image.

5.3.1 Particle Field Sizes

In order to accommodate the image sub-division process, the damage percolation software was modified to support "windowing" of the particle fields, such that smaller regions could be modelled. Given an initial point where the particle field

starts and the horizontal and vertical dimensions of the field, the percolation code
will read all the particle information of the field from the large field (parent field), as
depicted in Fig. 5.13. Particle field subsets were taken from the large
(4,250 × 5,500 pixel) image acquired for the as-received alloy. Calculations
were initially performed using particle fields that were 4,000 × 4,000 pixel in
size, taken from the larger acquired field. Given a pixel size of 0.372 μm, this
corresponds to a total image size of 1.49 × 1.49 mm. These larger images would
correspond to the largest area of interest (AOI) or representative volume element
(RVE) considered in this study.

To address the effect of RVE size, the original 4,000 × 4,000 pixel particle field
was divided into four equal-sized (2,000 × 2,000 pixel) sub-fields, and the damage
percolation simulation was repeated for each of these sub-fields. Next, the sub-
fields were further divided into 16 equal-sized (1,000 × 1,000 pixel) fields and then
into sixty-four 500 × 500 pixel fields, and again used for damage percolation
simulations. In principle, this sub-division process can be continued beyond this
field size; however, it was determined that subdivision of the image beyond the
sixty-four 500 × 500 pixel fields was not useful since catastrophic failure could not
be realized for some of these smaller fields for strains in excess 100 %, which
implies that the RVE should be at least larger than 500 × 500 pixels.

Table 5.1 lists the numbers of particles and initial particle areal fraction in the
larger 4,000 × 4,000 pixel images and the four sub-fields (from left to right, upper
to lower, denoted as a, b, c, and d). Table 5.2 gives the data for a selected
2,000 × 2,000 particle field and its four sub-fields. Both the number of particles
and areal fraction vary considerably between sub-fields. The data in Table 5.2 is
taken from the 2,000 × 2,000 pixel fields exhibiting failure strains closest to their
4,000 × 4,000 parent for all three loading cases.

Table 5.1 The effect of image size and particle number on the critical strain, AA5182 (4,000 pixel field) (Reprinted with permission from Worswick et al. (2001). Copyright: Elsevier)

Image size (pixel)	Number of particles	Initial particle areal fraction	Critical strain		
			Biaxial stretch	Uniaxial longitudinal	Uniaxial transverse
4,000	5,100	0.0162	0.3425	0.4275	0.3625
2,000a	1,254	0.0178	0.3425	0.4275	0.3625
2,000b	1,278	0.0167	0.395	0.4975	0.4325
2,000c	1,340	0.0152	0.4525	0.4925	0.4775
2,000d	1,228	0.0112	0.4425	0.4875	0.4925

Table 5.2 The effect of image size and particle number on the critical strain, AA5182 (2,000a) (Reprinted with permission from Worswick et al. (2001). Copyright: Elsevier)

Image size (pixel)	Number of particles	Initial particle areal fraction	Critical strain		
			Biaxial stretch	Uniaxial longitudinal	Uniaxial transverse
2,000a	1,254	0.0178	0.3425	0.4275	0.3625
1,000aa	310	0.017	0.415	0.4275	0.4375
1,000ab	348	0.0274	0.34	0.495	0.265
1,000ac	325	0.0154	0.485	0.7	0.43
1,000ad	271	0.0112	0.4925	1.3	1.05

5.3.2 Results and Discussion

The effect of the choice of representative volume element (RVE) is assessed in terms of the predicted strain to cause profuse void coalescence for different selected RVEs. For the purposes of this study, this limiting strain corresponds to the strain at which the crack areal fraction grows without further strain increment, as reflected by the steep vertical slopes seen in Figs. 5.11 and 5.12. This measure of limit strain to cause profuse coalescence is adopted to determine the influence of RVE size on the damage percolation predictions.

The limit strains at profuse coalescence for various particle fields are summarized in Tables 5.1 and 5.2. For the 2,000 × 2,000 pixel particle fields, profuse coalescence occurred in all the biaxial stretch and uniaxial cases. For the 2,000 × 2,000 fields, the critical strain level was in the range 0.34–0.44 for biaxial loading, compared to 0.43–0.50 and 0.36–0.49 for uniaxial loading in the longitudinal and transverse directions, respectively. It is worth noting that the critical strain for the 4,000 × 4,000 field was identical to those for its sub-field 2,000a which contains the particle clusters triggering the chain reaction associated with profuse void coalescence. Interestingly, this sub-field does not contain the largest number of particles when compared with its three sister-fields, but does exhibit the largest initial particle areal fraction of the four sub-fields. Figure 5.14a shows the predicted crack areal fraction using the larger AA5182 particle field (4,000 × 4,000 pixel) along with predictions from its smaller 2,000 × 2,000 pixel sub-fields (denoted as

Fig. 5.14 Predicted damage history for AA5182 under equi-biaxial stretching with (**a**) 4,000 × 4,000 pixels particle field and its sub-fields (2,000a, 2,000b, 2,000c, 2,000d); (**b**) 2,000 × 2,000 pixels particle field (2,000a) and its sub-fields (1,000aa, 1,000ab, 1,000ac, 1,000ad); (**c**) 1,000 × 1,000 pixels particle field (1,000aa) and its sub-fields (500aaa, 500aab, 500aac, 500aad) (Reprinted with permission from Worswick et al. (2001). Copyright: Elsevier)
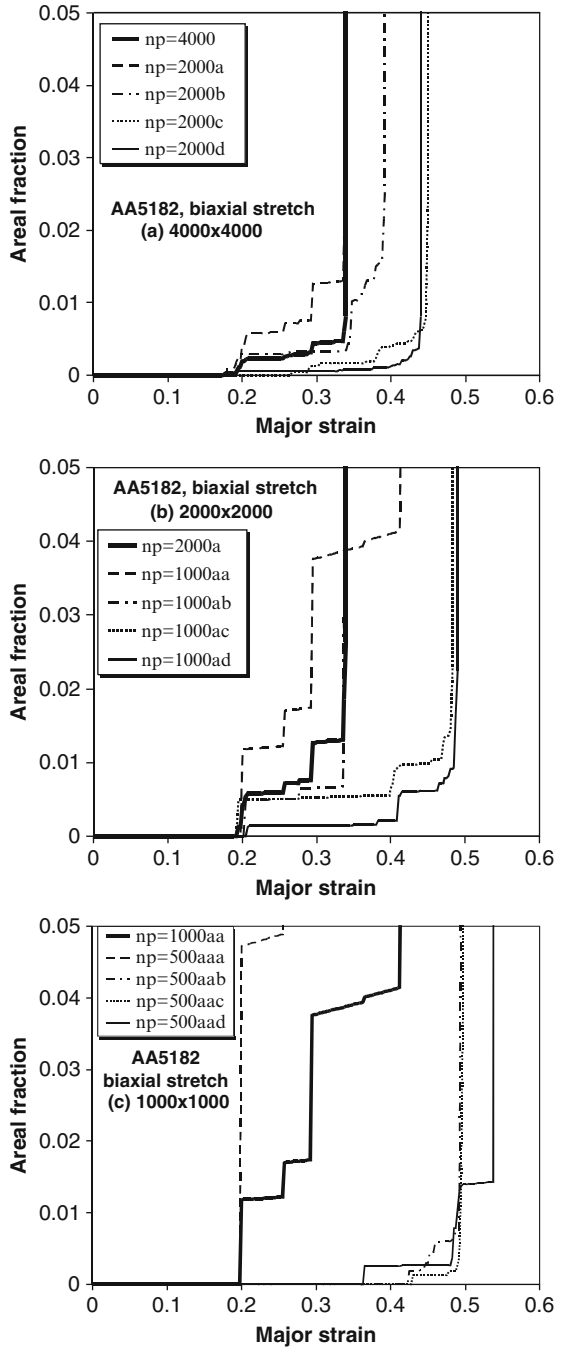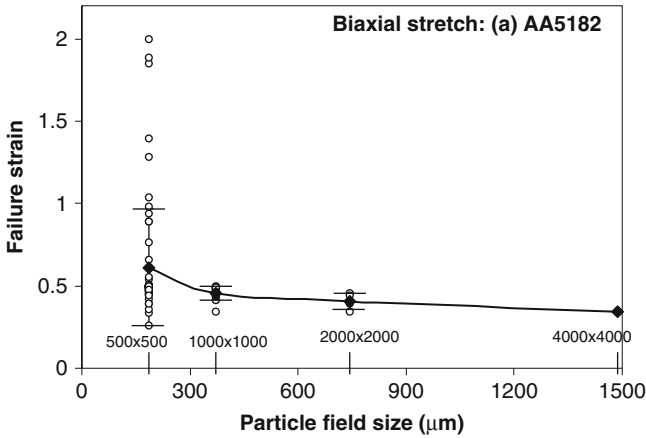
Fig. 5.15 Predicted failure strain (ductility) with RVE under biaxial stretching (Reprinted with permission from Worswick et al. (2001). Copyright: Elsevier)
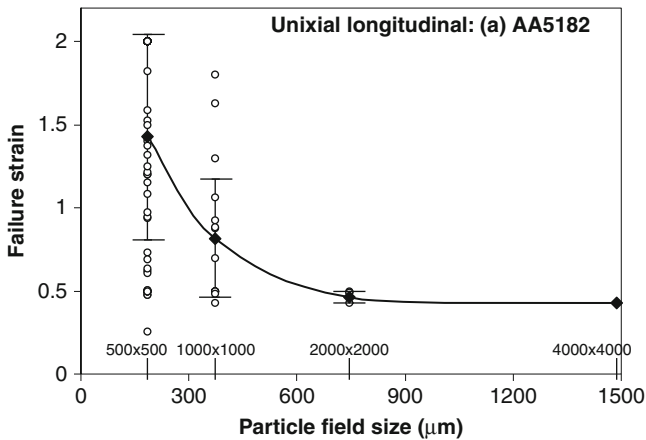

Fig. 5.16 Predicted failure strain (ductility) with RVE under longitudinal uniaxial stress condition. (**a**) AA5182 (Reprinted with permission from Worswick et al. (2001). Copyright: Elsevier)

2,000a–d in Table 5.1). The damage history of one of the smaller particle fields (2,000a) and its four sub-fields is plotted in Fig. 5.14b (Recall that this sub-field 2,000a contains the particle clusters that triggered the profuse coalescence in the 4,000 × 4,000 field simulation). To further illustrate the dependence of the predictions on RVE, the damage histories for a 1,000 × 1,000 pixel field (1,000aa) and its four sub-fields are plotted in Fig. 5.14c. It is evident that the degree of scatter in predicted failure strain increases as the size of the RVE is decreased as a natural consequence of sampling variability and the irregular particle distributions.
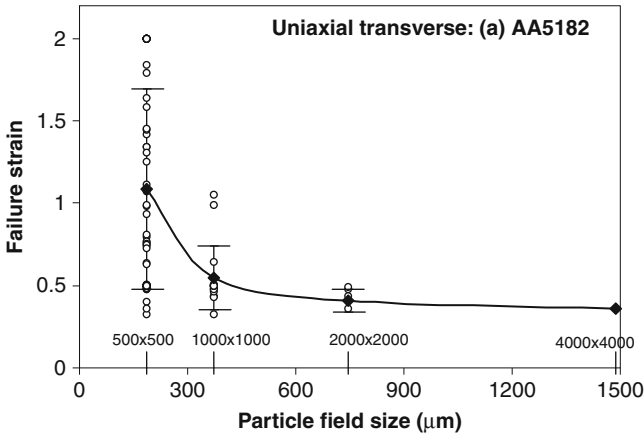
Fig. 5.17 Predicted failure strain (ductility) with RVE under transverse uniaxial stress condition (Reprinted with permission from Worswick et al. (2001). Copyright: Elsevier)

To further examine the variability in failure strain with RVE size, Fig. 5.15 plots the predicted failure strains as a function of RVE size under stretch loading (open symbols). The scatter bands in the figures correspond to the standard deviation in predicted failure strain and exhibit a very high dependence on RVE size. Note that in the calculations of variance, if the damage chain reaction did not occur when the applied strain reaches 2.0, the failure strain was taken as 2.0. Also plotted is the average value of failure strain versus RVE size (solid symbols). The degree of scatter for the predictions using the smallest RVE (500 × 500 pixels) is very high due to large sampling variability. The scatter is considerably reduced for the larger images and is similar for the 1,000 × 1,000 and 2,000 × 2,000 pixel fields. The corresponding results are plotted in Figs. 5.16 and 5.17 for longitudinal and transverse uniaxial loading, respectively. The dependence on RVE size is similar, however, the degree of scatter for the 1,000 × 1,000 pixel RVE is quite large for uniaxial loading compared to the stretch results in Fig. 5.15. This difference indicates that the rate of convergence in predicted ductility with increasing RVE size is slower for uniaxial loading. This behaviour is attributed to the constraint on coalescence given by Eq. (5.6), imposed for uniaxial loading that effectively limits the number of nearest neighbours that are candidates for coalescence compared to biaxial stretch loading for which coalescence can occur in any direction.

5.4 Summary

The validity of the damage percolation model in predicting ductile damage over the three distinct stages has been assessed with measured particle fields under various loading conditions. Damage percolation in second phase particle fields occurs as a

localized process, sensitive to initial particle clustering level, rather than a uniform process, as described in unit cell micromechanical models. Although introduction of particle clusters within a unit cell approach could somehow reveal the effect of interaction between particles and clusters (Thomson 2001), percolation simulations with actual measured particle fields do supply a more complete picture as to how void damage evolves in clustered particle fields to form a macrocrack. It is found that the void nucleation process dominates ductile damage within these aluminium alloys. The representative volume element study revealed that predicted ductility, in terms of the strain to cause profuse damage, shows a satisfactory convergence, for particle fields at least $2,000 \times 2,000$ pixels (0.75×0.75 mm) in size.